OEA | Opto-Electronic Advances

Dual-frequency angular-multiplexed fringe projection profilometry with deep learning: breaking hardware limits for ultra-high-speed 3D imaging

Wenwu Chen†, Yifan Liu†, Shijie Feng*, Wei Yin, Jiaming Qian, Yixuan Li, Hang Zhang*, Maciej Trusiak, Malgorzata Kujawinska, Qian Chen*, Chao Zuo*

https://doi.org/10.29026/oea.2025.250021

Opto-Electronic Advances

CN 51–1781/TN ISSN 2096–4579 (Print) ISSN 2097–3993 (Online)

Dual-frequency angular-multiplexed fringe projection profilometry with deep learning: breaking hardware limits for ultra-high-speed 3D imaging

Wenwu Chen, Yifan Liu, Shijie Feng, Wei Yin, Jiaming Qian, Yixuan Li, Hang Zhang, Maciej Trusiak, Malgorzata Kujawinska, Qian Chen and Chao Zuo

Citation: Chen WW, Liu YF, Feng SJ, et al. Dual-frequency angular-multiplexed fringe projection profilometry with deep learning: breaking hardware limits for ultra-high-speed 3D imaging. *Opto-Electron Adv* **8**, 250021(2025).

https://doi.org/10.29026/oea.2025.250021

Received: 12 February 2025; Accepted: 9 June 2025; Published online: 4 August 2025

Opto-Electronic Advances

Article

September 2025, Vol. 8, No. 9

DOI: 10.29026/oea.2025.250021 CSTR: 32247.14.oea.2025.250021

Dual-frequency angular-multiplexed fringe projection profilometry with deep learning: breaking hardware limits for ultra-high-speed 3D imaging

Wenwu Chen[1,3,4†], Yifan Liu[1,3,4†], Shijie Feng[1,3,4,5*], Wei Yin[1,3,4,5], Jiaming Qian[1,3,4,5], Yixuan Li[1,3,4,5], Hang Zhang[2*], Maciej Trusiak[6], Malgorzata Kujawinska[6], Qian Chen[4,5*] and Chao Zuo[1,3,4,5*]

Recent advancements in artificial intelligence have transformed three-dimensional (3D) optical imaging and metrology, enabling high-resolution and high-precision 3D surface geometry measurements from one single fringe pattern projection. However, the imaging speed of conventional fringe projection profilometry (FPP) remains limited by the native sensor refresh rates due to the inherent "one-to-one" synchronization mechanism between pattern projection and image acquisition in standard structured light techniques. Here, we present dual-frequency angular-multiplexed fringe projection profilometry (DFAMFPP), a deep learning-enabled 3D imaging technique that achieves high-speed, high-precision, and large-depth-range absolute 3D surface measurements at speeds 16 times faster than the sensor's native frame rate. By encoding multi-timeframe 3D information into a single multiplexed image using multiple pairs of dual-frequency fringes, high-accuracy absolute phase maps are reconstructed using specially trained two-stage number-theoretical-based deep neural networks. We validate the effectiveness of DFAMFPP through dynamic scene measurements, achieving 10,000 Hz 3D imaging of a running turbofan engine prototype with only a 625 Hz camera. By overcoming the sensor hardware bottleneck, DFAMFPP significantly advances high-speed and ultra-high-speed 3D imaging, opening new avenues for exploring dynamic processes across diverse scientific disciplines.

Keywords: 3D imaging; fringe projection profilometry; deep learning; multiplex; ultra-high-speed

Chen WW, Liu YF, Feng SJ et al. Dual-frequency angular-multiplexed fringe projection profilometry with deep learning: breaking hardware limits for ultra-high-speed 3D imaging. *Opto-Electron Adv* **8**, 250021 (2025).

[1]Smart Computational Imaging Laboratory (SCILab), School of Electronic and Optical Engineering, Nanjing University of Science and Technology, Nanjing 210094, China; [2]Key Laboratory of Shock Wave Physics and Detonation Physics, Institute of Fluid Physics, China Academy of Engineering Physics, Mianyang 621900, China; [3]Smart Computational Imaging Research Institute (SCIRI) of Nanjing University of Science and Technology, Nanjing 210019, China; [4]Jiangsu Key Laboratory of Visual Sensing & Intelligent Perception, Nanjing 210094, China; [5]State key Laboratory of Extreme Environment Optoelectronic Dynamic Measurement Technology and Instrument, Taiyuan 030051, China; [6]Institute of Micromechanics and Photonics, Warsaw University of Technology, 8 Sw. A. Boboli St., Warsaw 02-525, Poland.

[†]These authors contributed equally to this work.

*Correspondence: SJ Feng, E-mail: shijiefeng@njust.edu.cn; H Zhang, E-mail: zhanghang@caep.cn; Q Chen, E-mail: chenqian@njust.edu.cn; C Zuo, E-mail: zuochao@njust.edu.cn

Received: 12 February 2025; Accepted: 9 June 2025; Published online: 4 August 2025

Introduction

The concept of capturing and documenting fast events can date back to the earliest days of film photography[1]. With the advent of solid-state imaging technologies based on charge-coupled device (CCD) and complementary metal-oxide-semiconductor (CMOS) sensors, high-speed imaging has attracted increasing attention and interest[2]. Imaging techniques with high temporal resolution can "freeze" rapid motions and capture the transient changes of objects, offering unprecedented insights into scientific research. Over the past few decades, the need for high-speed, high-precision three-dimensional (3D) imaging has spanned diverse fields, including biomedical research[3], manufacturing[4], and aerospace engineering[5]. Concurrent advances in optoelectronics have driven rapid progress in 3D sensing technologies[6]. Among them, fringe projection profilometry (FPP) has been a cornerstone in non-contact 3D surface measurement due to its high spatial resolution and robustness[7,8].

The imaging speed of FPP is primarily constrained by two key factors: hardware limitations (the speed of the projector and camera) and algorithmic efficiency (the number of patterns required for each 3D reconstruction). On the hardware side, the development of binary defocusing techniques has significantly improved projection speed, achieving tens of kHz by defocusing the projector lens to produce quasi-sinusoidal fringes with 1-bit patterns[9,10]. On the algorithmic side, researchers have introduced various pattern schemes and decoding methods, such as dual-frequency phase shifting[11], 2+2 phase shifting[12], and bi-frequency phase shifting[13]. These approaches effectively reduce the number of patterns required for unambiguous 3D reconstruction by minimizing encoding redundancy. Recently, the rapid advancements in artificial intelligence (AI), particularly deep learning[14,15], have driven a paradigm shift in optical metrology[16]. Deep learning-based methods enable precise phase retrieval from a single fringe image[17,18]. Further integrating color fringes[19], geometric constraints[20], and frequency-domain multiplexing[21], high-precision absolute 3D imaging can be achieved from a single shot. However, the "one-to-one" synchronization between pattern projection and image acquisition has long hindered the temporal resolution of conventional FPP techniques. The imaging speed remains constrained by the native rate of sensors, limiting its application in dynamic scenarios. Current efforts to enhance speed rely on high-refresh-rate hardware, which significantly increases system complexity and cost[22,23].

To address these limitations, researchers have combined compressive sensing[24–26] with computational imaging[27,28], developing a series of temporal super-resolution imaging techniques, such as compressed ultrafast photography (CUP)[29], coded aperture compressive temporal imaging (CACTI)[30], and programmable pixel compressive camera (P2C2)[31]. However, these techniques typically rely on complex optical modulation hardware, which complicates optical system design and causes unavoidable photon loss, resulting in low signal-to-noise ratios (SNRs) of the reconstructed images. Moreover, these methods are primarily designed for two-dimensional (2D) imaging. Extending them to 3D sensing imposes additional burdens on the optical setup and reconstruction algorithms. Recent advances in deep learning pave new paths for solving complex imaging challenges by leveraging data-driven models to overcome hardware constraints[32–35]. Among these efforts, deep-learning-enabled multiplexed FPP (DLMFPP)[34] allows to achieve 9× temporal super-resolution 3D imaging using two low-speed cameras, eliminating the need for optical modulators and enabling implementation on almost any off-the-shelf FPP system. Nevertheless, whether 3D imaging can be pushed to even higher temporal resolutions remains an open question and a persistent focus of researchers. Furthermore, DLMFPP relies on the conventional stereo phase unwrapping (SPU) algorithm[36,37] to obtain absolute phase maps. However, SPU typically struggles to reliably unwrap dense fringes, which severely constrains the use of higher-frequency fringes—crucial for mitigating aliasing of fundamental frequencies in multiplexed spectra and for enhancing measurement accuracy. Therefore, DLMFPP enforces strict depth constraints[38,39] and requires at least two cameras for geometric relationships to improve the robustness of phase unwrapping to some extent. These limitations, including reduced measurement range and precision, along with the elevated costs of multi-camera setups, currently hinder the widespread application of DLMFPP in high-speed and ultra-high-speed 3D imaging scenarios.

Building on this, in this work, we introduce dual-frequency angular-multiplexed fringe projection profilometry (DFAMFPP), a novel deep learning-enabled technique that decouples the speed limitation imposed by traditional FPP systems, using a single camera to provide high-speed, high-precision, and large-depth-range

absolute 3D shape measurement. This method encodes multi-timeframe 3D information into a single multiplexed image using carefully designed dual-frequency fringe patterns, achieving 16× temporal super-resolution without compromising spatial resolution. We demonstrate the effectiveness of DFAMFPP by conducting dynamic scene measurements, achieving 10,000 Hz 3D imaging of a running turbofan engine prototype using only a 625 Hz camera. DFAMFPP is expected to invigorate the development of high-speed and ultra-high-speed 3D imaging capabilities, breaking through the sensor hardware bottleneck, and driving progress in multiple research fields.

Methods

Fringe pattern design and projection

The DFAMFPP system utilizes multiple pairs of dual-frequency fringe patterns, with each pair consisting of high- and low-frequency components projected at specific angular orientations. The high-frequency fringes encode fine spatial details, while the low-frequency fringes provide global unwrapping information. By modulating the projection sequence at speeds exceeding the native camera frame rate, temporal multiplexing is achieved. The schematic illustration of the DFAMFPP method is shown in Fig. 1, in which a rotating "David" plaster statue is employed as the dynamic scene to illustrate the principle. In DFAMFPP, the projector casts M pairs of dual-frequency fringe patterns onto the rotating "David" sequentially. The specially designed fringe pattern I_m^{p} can be expressed as:

$$I_m^{\mathrm{p}}\left(x^{\mathrm{p}}, y^{\mathrm{p}}\right) = a + b\cos\left[\varphi_m\left(x^{\mathrm{p}}, y^{\mathrm{p}}\right)\right] , \tag{1}$$

where $a = b = 0.5$ are the mean and amplitude, respectively, $(x^{\mathrm{p}}, y^{\mathrm{p}})$ represents the pixel coordinate on the projector, and the subscript m denotes the projected pattern index where $m = 1, 2, 3, \ldots, 2M$. In addition, an auxiliary variable n is introduced, which represents the pattern pair index ($n = 1, 2, 3, \ldots, M$), and the phase φ_m is set to:

$$\varphi_m(x^{\mathrm{p}}, y^{\mathrm{p}}) = \begin{cases} 2\pi(x^{\mathrm{p}}\cos\theta_n/\lambda_x^{\mathrm{l}} + y^{\mathrm{p}}\sin\theta_n/\lambda_y^{\mathrm{l}}) & m = 2n-1 \\ 2\pi(x^{\mathrm{p}}\cos\theta_n/\lambda_x^{\mathrm{h}} + y^{\mathrm{p}}\sin\theta_n/\lambda_y^{\mathrm{h}}) & m = 2n \end{cases}, \tag{2}$$

$$\theta_n = (-1)^{n+1}\left(\frac{n}{2} - \frac{(-1)^n + 1}{4}\right)\theta, \tag{3}$$

where λ_x^{l} and λ_y^{l} represent the wavelengths of the low-frequency fringes in the x and y directions respectively, and λ_x^{h} and λ_y^{h} are the wavelengths of the high-frequency ones. It is worth noting that for a projection pattern of $H \times W$, the wavelengths need to satisfy $LCM(\lambda_x^l, \lambda_x^h) \geq W$ and $LCM(\lambda_y^l, \lambda_y^h) \geq H$ (where LCM() denotes the least common multiple) to ensure that the entire projection

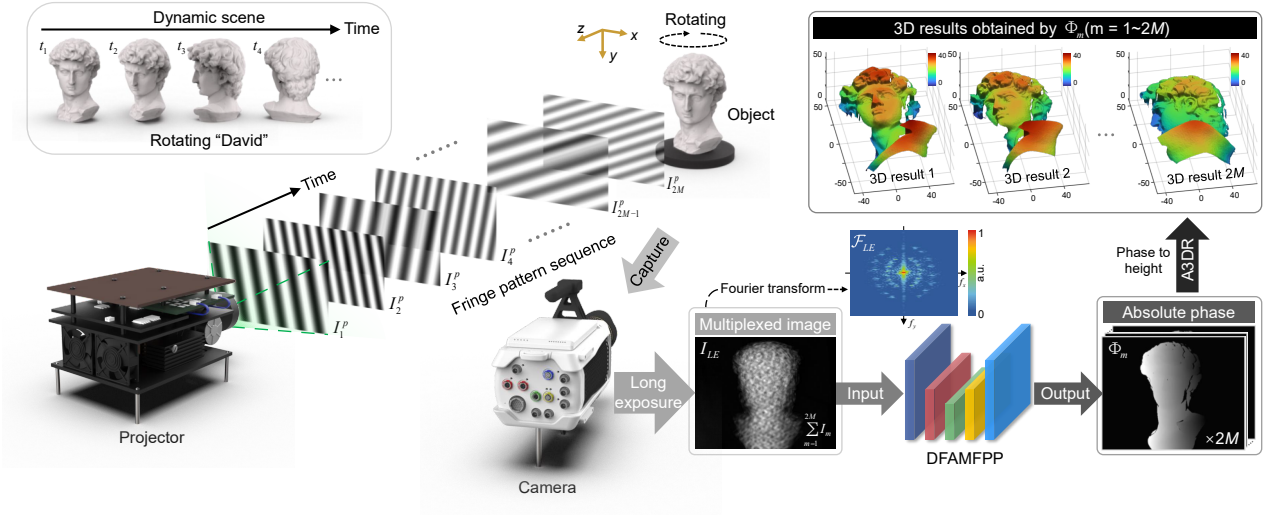

Fig. 1 | Schematic illustration of DFAMFPP. The projector casts M pairs of specially designed dual-frequency fringe patterns I_m^{p} onto a dynamic scene (a rotating "David" plaster statue) sequentially. Then the camera captures a multiplexed image I_{LE} of multiple fringes overlapped through a long exposure time, encoding the 3D information of the scene at $2M$ consecutive moments. After Fourier transform, the scene information at different times presents a special pattern of a pair of concentric circles in the spatial spectrum. DNNs in DFAMFPP can further be employed to decompose a frame of multiplexed image I_{LE} into $2M$ frames of absolute phase maps Φ_m. Finally, 3D results can be obtained by proper calibration and the A3DR phase-to-depth algorithm.

area lies within the effective disambiguation range of the number-theoretical phase unwrapping[40]. θ is a scalar characterizing the specific angular orientation of the fringe. When the fringe pattern I_m^{p} is projected onto the object and modulated by the measured surface, the image intensity corresponding to I_m^{p} can be represented as:

$$I_m(x,y) = A(x,y) + B(x,y)\cos[\phi_m(x,y)], \tag{4}$$

where (x, y) represents the pixel coordinate of the camera (omitted below for brevity), A and B are the average intensity and modulation, respectively, and ϕ_m denotes the modulated phase.

Specifically, the modulated fringe images I_m carry the 3D information of the measured dynamic scene at different times, that is the 3D shape of the rotating "David" at different perspectives in Fig. 1. Note that in DFAMFPP, the camera captures a multiplexed image I_{LE} of multiple overlapped images I_m through a long exposure time, which can be expressed as:

$$I_{\mathrm{LE}} = I_1 + I_2 + \ldots + I_{2M} = \sum_{m=1}^{2M} I_m, \tag{5}$$

which contains the 3D scene information at $2M$ consecutive moments. After Fourier transforming I_{LE}, the 3D information at different times is distributed in distinct regions of the spatial spectrum; the dual-frequency fringes present a special pattern of a pair of concentric circles. Notably, a single pair of dual-frequency fringes provides sufficient information required for phase unwrapping using the number-theoretical method. Moreover, the number-theoretical approach is not subject to the strict constraints on fringe frequency and depth range typically imposed by SPU. Therefore, we can use the specially trained two-stage deep neural networks (DNNs) to reconstruct $2M$ frames of high-accuracy absolute phase maps Φ_m from a single multiplexed image. Combined with proper calibration and the developed augmented 3D reconstruction (A3DR) algorithm for phase-to-depth mapping, temporal super-resolution, high-precision, and large-depth-range 3D imaging at speeds $2M\times$ higher than the camera's native frame rate can be achieved. Details of the system calibration and the A3DR method are provided in Supplementary information, Sections 1 and 2.

Deep neural network architecture

The reconstruction flowchart of DFAMFPP is detailed in Fig. 2. Overall, we developed a preprocessing and two-stage deep learning framework to decode multiplexed images into high-accuracy phase maps, consisting of three steps: Step 0. Zero-order removal (ZOR) preprocessing removes the zero-order part of the multiplexed

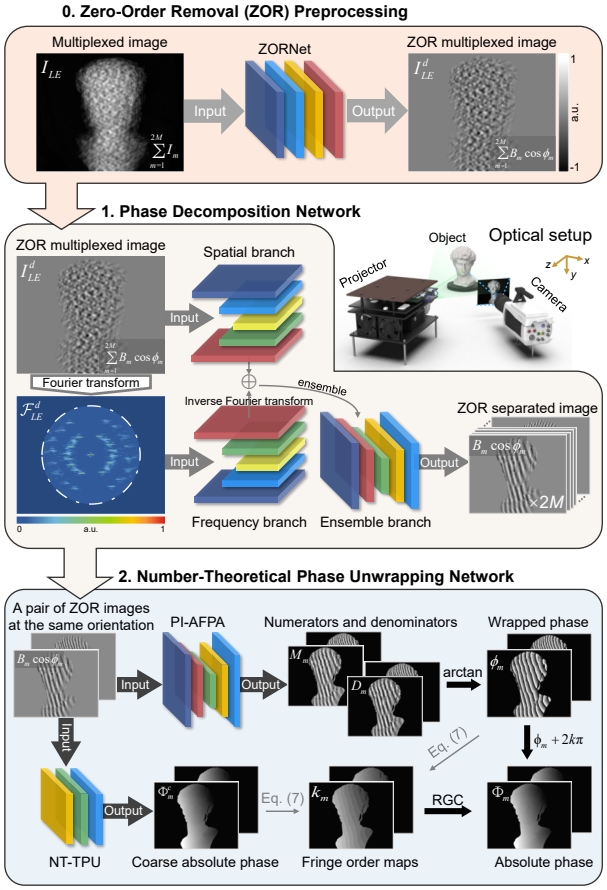

Fig. 2 | Reconstruction flowchart of the DFAMFPP method, consisting of three steps: ZOR preprocessing, Phase decomposition network and number-theoretical phase unwrapping network. Step 0 employs ZORNet, a learning-enhanced high-pass filter, to remove the zero-order part of the multiplexed image I_{LE}, and obtains the ZOR multiplexed image $I_{\mathrm{LE}}^{\mathrm{d}}$, containing only high-frequency components encoding 3D scene information at different times. Step 1 extracts the features of the ZOR multiplexed image $I_{\mathrm{LE}}^{\mathrm{d}}$ in both the spatial and frequency domains through a spatial-frequency hybrid DNN composed of three branches: spatial, frequency, and ensemble parts, to output a high-quality image sequence, the ZOR separated images $B_m\cos\phi_m$. Step 2 employs PI-AFPA, a physics-informed fringe analysis module, and NT-TPU, a learning-enhanced number-theoretical unwrapping module, to perform phase analysis and unwrapping. PI-AFPA processes a pair of dual-frequency ZOR images in the same orientation to predict the corresponding high-precision numerator M_{m} and denominator D_m terms of the wrapped phase ϕ_m. NT-TPU takes in the same pair of images and outputs coarse absolute phase maps Φ_m^c, which can obtain the accurate fringe order map k_m with the help of ϕ_m through Eq. (7). By further incorporating the RGC algorithm, high-precision absolute phase maps ϕ_m for 3D reconstruction can finally be provided.

image, retaining the high-frequency components that encode the 3D scene information at different times. Step 1. Phase decomposition network separates the multiplexed image into individual fringe components using a spatial-frequency hybrid architecture. Step 2. Number-theoretical phase unwrapping network reconstructs high-precision absolute phase maps by leveraging number-theoretical constraints and physics-informed priors. Details are as follows:

Step 0: We noticed that in the multiplexed spectrum ($\mathcal{F}_{\rm LE}$ in Fig. 1), there is aliasing between the zero-order and multiple high-frequency components, which can be more serious on complex surfaces and discontinuous areas. Importantly, the high-frequency components encode the 3D information of the dynamic scene at different times, while the zero-order component makes no contribution to the final 3D recovery. Therefore, we constructed a ZORNet, a learning-enhanced high-pass filter constructed by Multi-path convolutional neural network (CNN)[41], which can obtain the ZOR multiplexed image $I_{\rm LE}^{\rm d}=\sum_{m=1}^{2M}B_m\cos\phi_m$ from the input multiplexed image $I_{\rm LE}$. The ZORNet can effectively remove the zero-order part in $I_{\rm LE}$, making the subsequent decomposition of the multiplexed image more efficient and maintaining high accuracy. More details about the Multi-path CNN architecture can be found in Supplementary information Section 3.

Step 1: In the phase decomposition, we construct a spatial-frequency hybrid DNN consisting of three branches: spatial, frequency, and ensemble parts[34,42], all based on the MultiResUnet architecture[43] (see Supplementary information, Section C for the detailed MultiResUnet structure). The spatial branch receives the ZOR multiplexed image $I_{\rm LE}^{\rm d}$ and extracts spatial domain features; the frequency branch receives the multiplexed spectrum $\mathcal{F}_{\rm LE}^{\rm d}$ (Fourier transform of $I_{\rm LE}^{\rm d}$) and extracts frequency domain features; the ensemble branch adaptively integrates the features of both domains and outputs a high-quality image sequence, the ZOR separated images $B_m\cos\phi_m$.

Step 2: In the number-theoretical phase unwrapping, we constructed two DNNs: physics-informed augmented fringe pattern analysis (PI-AFPA) constructed by U-Net[44] and number-theoretical temporal phase unwrapping (NT-TPU) constructed by Multi-path CNN, to perform fringe analysis and phase unwrapping respectively. Further details regarding the network architectures are provided in Supplementary information Section C. Inspired by the physical model empowering deep learning[18,45,46], we constructed PI-AFPA to perform high-precision phase recovery on ZOR images. PI-AFPA combines the physical prior knowledge of traditional Fourier transform profilometry (FTP) and phase shifting method, and can receive a pair of dual-frequency ZOR images in the same orientation to predict the corresponding high-precision numerator M_m and denominator D_m terms[17]. Then the accurate wrapped phase ϕ_m (in Eq. (4)) can be obtained by

$$\phi_m=\arctan\frac{M_m}{D_m}\,, \tag{6}$$

with physics-informed priors, PI-AFPA can achieve accurate and efficient phase retrieval, providing a guarantee for reliable 3D reconstruction. Subsequently, for phase unwrapping, NT-TPU receives the same pair of images and outputs the corresponding coarse absolute phase maps $\Phi_m^{\rm c}$. Although influenced by ambient light, large surface reflectivity and discontinuity, it is difficult for NT-TPU to directly obtain high-quality absolute phase information. The accurate fringe order map k_m can be obtained by Eq. (7):

$$k_m=\text{Round}\left(\frac{\Phi_m^{\rm c}-\phi_m}{2\pi}\right)\,, \tag{7}$$

with k_m, the high-precision absolute phase Φ_m can be solved by $\Phi_m=\phi_m+2k_m\pi$[19]. Note that the input pair of ZOR images corresponds to different times, leading to a small range of unwrapping errors at the object edge. To address this, the DFAMFPP method employs the reliability-guided compensation (RGC) algorithm[22], effectively mitigating these errors and yielding a high-precision, robust absolute phase map Φ_m. By further incorporating calibration parameters and the A3DR algorithm, the absolute 3D shape can be accurately reconstructed.

Experimental setup

We established the experimental system shown in the inset of Fig. 2, comprising a scientific CMOS camera (Vision Research Phantom V611) and a digital micro-mirror device (DMD) projection system. The projection system is composed of a digital light processing (DLP) development kit (Texas Instruments DLP Discovery 4100) with an XGA resolution (1024×768) DMD, coupled with a custom-designed optical module. The DMD operates in binary mode at 1,600 Hz (with an available resolution of 1024×512), while the camera captures images at 100 Hz with an exposure time synchronized to the projection

sequence (i.e., the projection system output a trigger signal to the camera every 16 frames, with M set to 8). The camera operated at an image resolution (640×440) with a pixel depth of 16 bits. Specifically, in the fringe design, the wavelengths in Eq. (2) is set to $\lambda_x^l = 43$, $\lambda_x^h = 24$, $\lambda_y^l = 31$, and $\lambda_y^h = 17$, where $LCM(\lambda_x^l, \lambda_x^h) = 1032$, $LCM(\lambda_y^l, \lambda_y^h) = 527$. More discussions on the wavelength selection for dual-frequency fringes are provided in the Supplementary information Section 5. Calibration involves mapping each camera pixel to the projector coordinate system using a 9×11 calibration board. For further information on the system calibration, please see Supplementary information Section 1. In addition, the networks are trained on a synthetic dataset generated using simulated and real fringe patterns, along with their corresponding ground-truth phase maps to ensure generalization across varying scene conditions. More details on network training and dataset preparation are provided in Supplementary information Section 4.

Results

To demonstrate the temporal super-resolution imaging capability of the DFAMFPP method, we performed 3D videography of a fast-changing dynamic scene: a four-blade fan rotating at ~4,800 revolutions per minute (RPM). The complete process of the method is shown in Fig. 3(a). The captured raw multiplexed image I_{LE} was filtered in Step 0 to obtain the corresponding ZOR multiplexed image $I_{\mathrm{LE}}^{\mathrm{d}}$ and its spatial spectrum $\mathcal{F}_{\mathrm{LE}}^{\mathrm{d}}$, in which the zero-order component is effectively removed. Subsequently, $I_{\mathrm{LE}}^{\mathrm{d}}$ was decomposed after Step 1, and output the ZOR separated images $B_m\cos\phi_m$, where $m = 1, 2, 3, \ldots, 16$ (the background is partially transparent for better visualization). Step 2 finally analyzed and unwrapped the phase to produce the corresponding high-precision absolute phase maps Φ_m. Although the raw multiplexed image I_{LE} suffers from severe motion blur, the 3D geometry of the entire fan was well-resolved by DFAMFPP, as

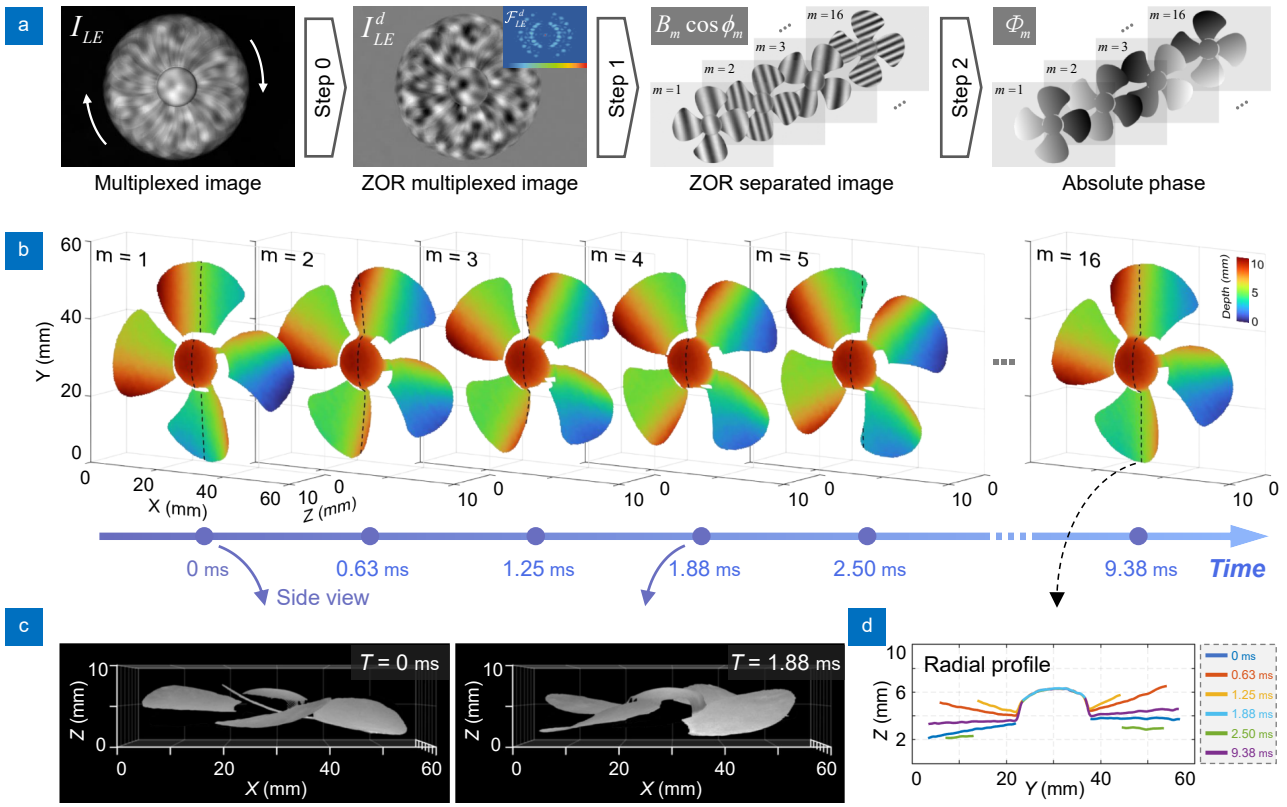

Fig. 3 | Dynamic measurement of a rotating four-blade fan. (**a**) The complete process of the DFAMFPP method. The camera captured the raw multiplexed image I_{LE} through a long exposure shot. Step 0 removed the zero-order component to obtain the ZOR multiplexed image $I_{\mathrm{LE}}^{\mathrm{d}}$ and its spatial spectrum $\mathcal{F}_{\mathrm{LE}}^{\mathrm{d}}$ (partial zoom display). Step 1 decomposed $I_{\mathrm{LE}}^{\mathrm{d}}$ to output ZOR separated images $B_m\cos\phi_m$, where m=1,2,3,...,16 (the background is partially transparent for better visualization). Step 2 finally analyzed and unwrapped the phase to provide high-quality absolute phase maps Φ_m. (**b**) The color-coded 3D rendering of the fan surface at different times (T = 0, 0.63, 1.25, 1.88, 2.50,..., 9.38 ms). (**c**) Side-view of the fan at T = 0 ms and 1.88 ms, rendered by grayscale. (**d**) Height curves plotted along the radial profile at different times (corresponding to the dashed line in (b)).

shown in Fig. 3(b), which presents the color-coded 3D rendering of the fan surface at different times (where T = 0, 0.63, 1.25, 1.88, 2.50, ..., 9.38 ms). It is worth noting that the DFAMFPP method fundamentally addresses motion blur through its unique mechanism of first capturing long-exposure multiplexed images and subsequently decomposing them. Specifically, the effective exposure time of each individual fringe image is governed by the projection duration of the corresponding pattern, rather than the camera's exposure time. As a result, the motion blur observed in the reconstructed 3D frames is governed solely by the projection time of the projector system. Consequently, even though the raw multiplexed image I_{LE} exhibits significant motion blur, DFAMFPP is capable of resolving the temporal positional variations of the rotating fan blades accurately. Figure 3(c) demonstrates the side-view (x-z) of the fan 3D reconstruction at T = 0 ms and 1.88 ms, rendered by the corresponding grayscale. Moreover, in Fig. 3(d), we plot radial profiles through the central hub of the fan (corresponding to the dashed line in (b)). In one multiplexed frame (within 9.38 ms), the fan rotates nearly 1/2 of a turn, exhibiting a maximum depth variation exceeds 3.5 mm in the z-direction.

To further verify the scalability of DFAMFPP in terms of imaging speed, we adjusted the projection speed to 10,000 Hz and the camera frame rate to 625 Hz. The previously trained DNNs were directly utilized to perform 3D measurements. We used the system to capture a running turbofan engine prototype rotating at ~9,500 rpm. Despite severe motion blur in raw images, DFAMFPP successfully reconstructed the 3D surface at 10,000 Hz temporal resolution. Figure 4 illustrates the sequential reconstructions, highlighting the technique's ability to resolve high-speed dynamics. The raw multiplexed image captured by the camera, I_{LE}, is shown in Fig. 4(a), along with the corresponding ZOR multiplexed image and its spectrum. Despite the complete distortion of the high-speed rotating turbofan blades due to the superposition of fringe images, the DFAMFPP successfully resolved the 3D shape of the blades, as shown in Fig. 4(b). To assess the reliability of our method for temporal

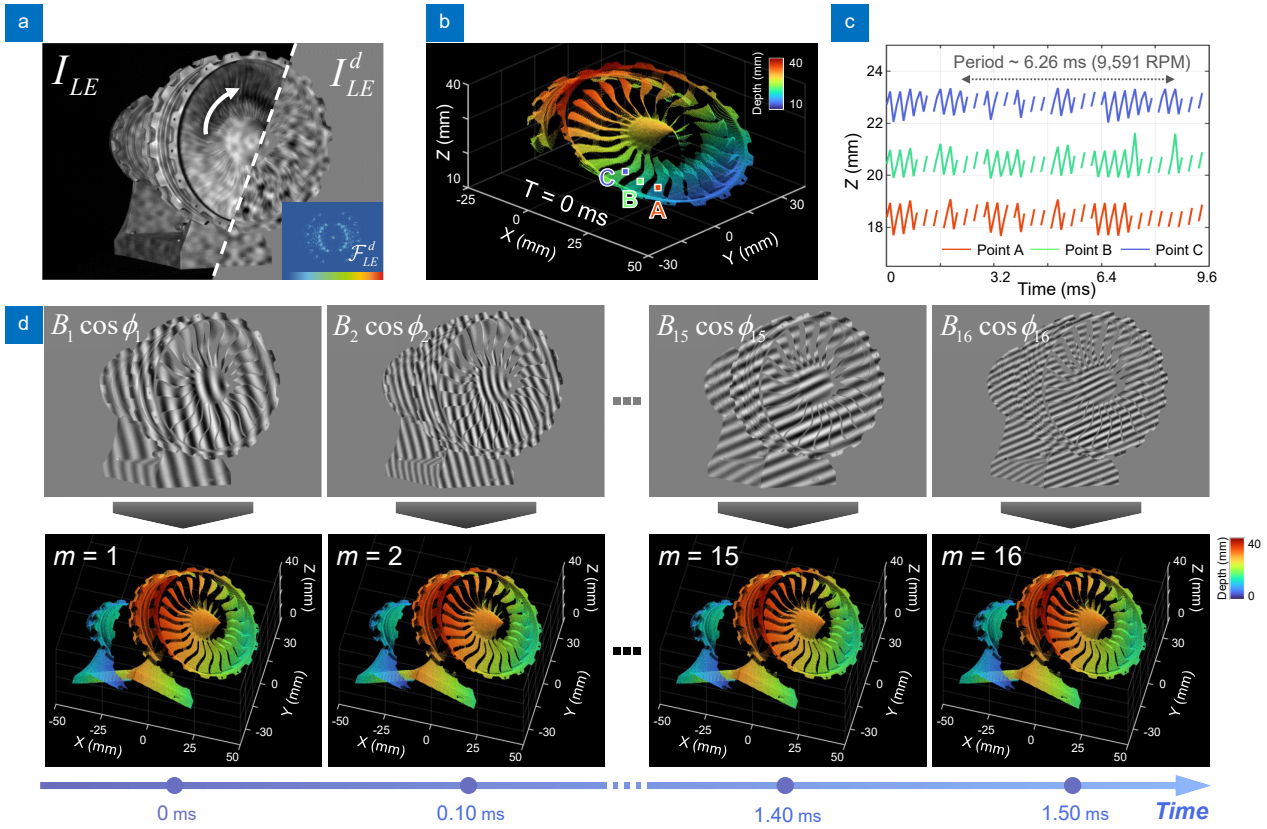

Fig. 4 | Dynamic measurement of a running turbofan engine prototype. (**a**) The raw multiplexed image I_{LE} captured by the camera, along with the corresponding ZOR multiplexed image and its spectrum. (**b**) The color-coded 3D rendering of the turbofan blades at T = 0 ms. (**c**) Displacement along the z-direction at 3 selected point locations (A, B, and C in b) over a period of 9.6 ms. (**d**) ZOR separated images $B_m\cos\phi_m$ (m = 1, 2, 3, ..., 16, at T = 0, 0.10, 0.20,..., 1.50 ms) decoded from a single multiplexed frame (I_{LE} in (a)), along with their corresponding color-rendered 3D models.

super-resolution imaging, we selected three arbitrary points on the blades, labeled A, B, and C in Fig. 4(b), to illustrate the periodic rotation. Figure 4(c) plots the displacement along the z-direction at these three locations over a period of 9.6 ms, demonstrating a rotation period of approximately 6.26 ms, corresponding to a rotational speed of 9,591 rpm. Figure 4(d) presents the four ZOR separated images, $B_m\cos\phi_m$ ($m = 1, 2, 15, 16$, at times T = 0, 0.10, 1.40, and 1.50 ms), decoded from a single multiplexed frame (I_{LE} in Fig. 4(a)), along with their corresponding color-rendered 3D models. The complete process of DFAMFPP and 3D results of the entire dynamic turbine engine process is provided in Visualization S1. Experimental results and analysis confirm that the DFAMFPP technique can retrieve 16 3D images from each multiplexed frame, achieving high-speed 3D imaging at up to 10,000 Hz using a 625 Hz camera.

To quantitatively evaluate the measurement accuracy of the proposed DFAMFPP method, we further conducted an experiment to measure a pair of calibrated standard ceramic spheres (Radius A: 25.3967 mm; Radius B: 25.3989 mm) with a center-to-center distance of 100.1166 mm (certified by a coordinate measuring machine), as shown in Fig. 5(a). Figure 5(b) presents the captured multiplexed image, ZOR-processed image, and corresponding spatial frequency spectrum (with local magnification for enhanced visualization). The 3D reconstruction results and their error distributions at two different positions are shown in Figs. 5(c, d). Measurement accuracy was quantified by calculating the discrepancy between the reconstructed 3D data and ground truth obtained through least-squares sphere fitting of the point clouds. At Position 1 (Fig. 5(c)), the root mean square errors (RMSE) for sphere radius measurements were 90.1746 μm and 98.0895 μm, with a mean absolute error (MAE) of 64.3268 μm for center-to-center distance.

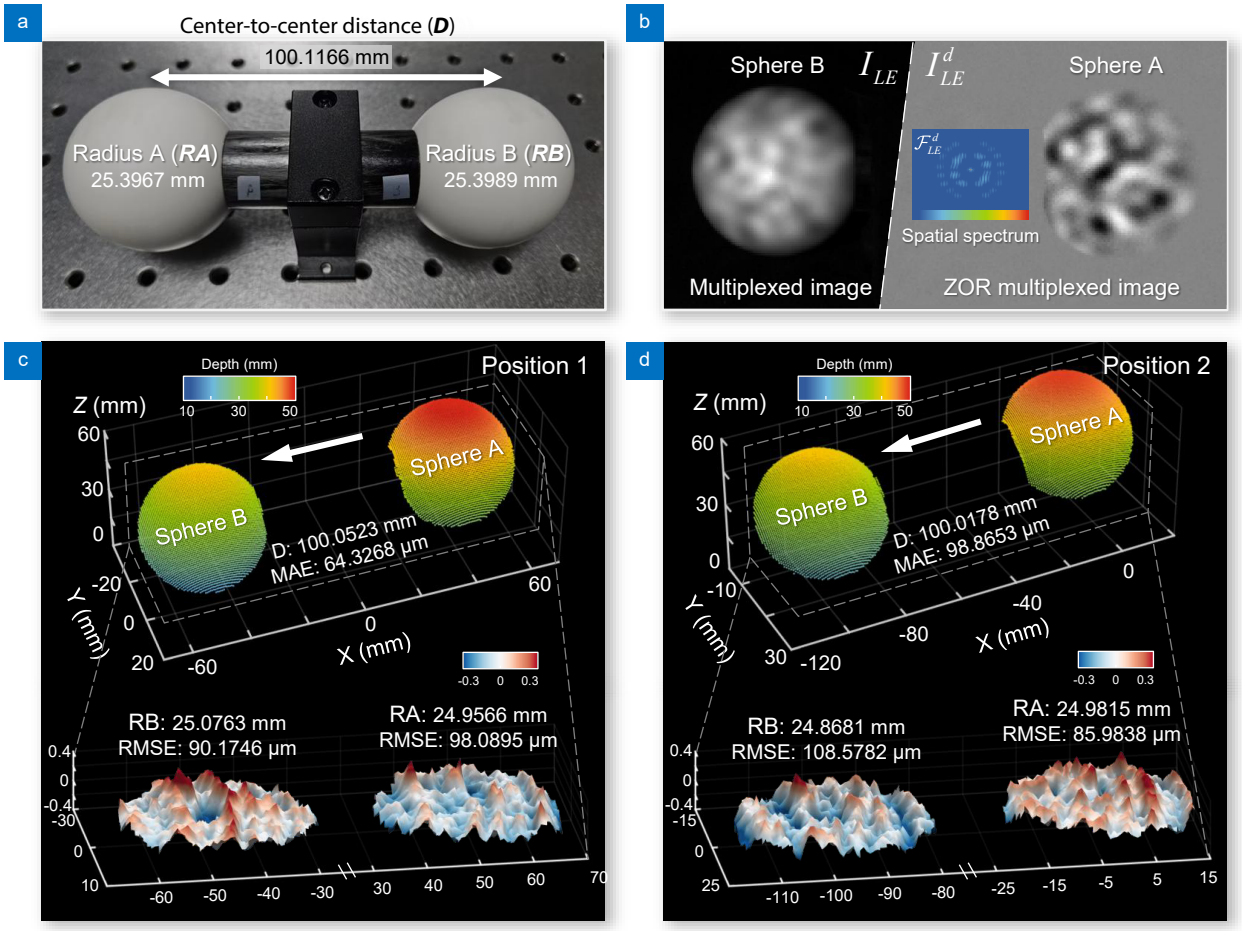

Fig. 5 | Accuracy analysis of 3D measurement using DFAMFPP. (**a**) A measurement scenario involving a pair of standard ceramic spheres with corresponding standard parameters. (**b**) The scene-modulated multiplexed image and the corresponding spatial frequency spectrum (with local magnification for enhanced visualization). (**c**, **d**) The color-coded 3D rendering, error distributions maps of the standard spheres at two distinct positions.

Position 2 (Fig. 5(d)) exhibited similar precision, with average radius measurement RMSE of 97.2812 μm and center-to-center distance MAE of 98.8653 μm. These results confirm DFAMFPP's capability for absolute 3D measurements with better than 100 μm accuracy. Additionally, we acknowledge that this performance benchmark was achieved under ideal conditions with simple geometric shapes. The standard spheres inherently minimize spectral aliasing and crosstalk between high-frequency components in the multiplexed spectrum, thereby facilitating higher measurement precision than might be expected with complex geometries. This establishes an upper bound for the system's measurement capability under optimal conditions. In addition, to further demonstrate the advancement of the DFAMFPP method, in Supplementary information Section 6, we present additional comparative studies with the traditional FTP method and the previous DLMFPP method. These results confirm DFAMFPP's capability for high-speed, high-precision, and large-depth-range 3D imaging while significantly exceeding the camera's native frame rate limitations.

Discussion and conclusion

This study presents DFAMFPP, a novel deep learning-enabled technique for high-speed 3D imaging. By achieving 16× temporal super-resolution and overcoming sensor hardware limitations, DFAMFPP significantly advances the state of the art in FPP. Its capability to capture ultra-high-speed dynamics holds promise for transformative applications in scientific research and industrial inspection.

Despite the impressive progress of DFAMFPP in high-speed 3D imaging, several inherent limitations remain. The maximum imaging speed is fundamentally limited by the refresh rate of the projector, as the modulation speed of 3D information is inherently bounded by the projector's switching capability. In addition, there exists a trade-off between the information content of each decomposed frame and the number of multiplexed projections: increasing the temporal super-resolution ratio often compromises the final measurement accuracy, whereas emphasizing reconstruction accuracy constrains the achievable temporal resolution.

The proposed DFAMFPP method addresses the long-standing hardware bottleneck in FPP by introducing a computational framework that leverages the synergy between physics-informed modeling and deep learning. The dual-frequency angular-multiplexing strategy ensures robust phase unwrapping even under challenging conditions, such as high-speed motion or low signal-to-noise ratios. Potential limitations include the reliance on precise calibration and the computational cost of deep learning inference. Future work could focus on hardware acceleration[47,48] and real-time implementation[28,49] to further broaden its applicability.

References

1. Lunn GH. High-speed photography. *Nature* **291**, 617–619 (1981).
2. Kleinfelder S, Lim S, Liu XQ et al. A 10000 frames/s CMOS digital pixel sensor. *IEEE J Solid-State Circuits* **36**, 2049–2059 (2001).
3. Ford KR, Myer GD, Hewett TE. Reliability of landing 3D motion analysis: implications for longitudinal analyses. *Med Sci Sports Exerc* **39**, 2021–2028 (2007).
4. Malamas EN, Petrakis EGM, Zervakis M et al. A survey on industrial vision systems, applications and tools. *Image Vis Comput* **21**, 171–188 (2003).
5. Xi XL, Liu Y, Xue P et al. High-speed multi-camera videogrammetric measurement of full-field 3D motion and deformation in full-scale crash testing of typical civil aircraft. *Aerosp Sci Technol* **152**, 109375 (2024).
6. Geng JS. Structured-light 3D surface imaging: a tutorial. *Adv Opt Photonics* **3**, 128–160 (2011).
7. Gorthi SS, Rastogi P. Fringe projection techniques: whither we are. *Opt Lasers Eng* **48**, 133–140 (2010).
8. Zuo C, Feng SJ, Huang L et al. Phase shifting algorithms for fringe projection profilometry: a review. *Opt Lasers Eng* **109**, 23–59 (2018).
9. Li BW, Wang YJ, Dai JF et al. Some recent advances on superfast 3D shape measurement with digital binary defocusing techniques. *Opt Lasers Eng* **54**, 236–246 (2014).
10. Zuo C, Chen Q, Feng SJ et al. Optimized pulse width modulation pattern strategy for three-dimensional profilometry with projector defocusing. *Appl Opt* **51**, 4477–4490 (2012).
11. Liu K, Wang YC, Lau DL et al. Dual-frequency pattern scheme for high-speed 3-D shape measurement. *Opt Express* **18**, 5229–5244 (2010).
12. Zuo C, Chen Q, Gu GH et al. High-speed three-dimensional profilometry for multiple objects with complex shapes. *Opt Express* **20**, 19493–19510 (2012).
13. Zuo C, Chen Q, Gu GH et al. High-speed three-dimensional shape measurement for dynamic scenes using bi-frequency tripolar pulse-width-modulation fringe projection. *Opt Lasers Eng* **51**, 953–960 (2013).
14. LeCun Y, Bengio Y, Hinton G. Deep learning. *Nature* **521**, 436–444 (2015).
15. Schmidhuber J. Deep learning in neural networks: an overview. *Neural Netw* **61**, 85–117 (2015).
16. Zuo C, Qian JM, Feng SJ et al. Deep learning in optical metrology: a review. *Light Sci Appl* **11**, 39 (2022).
17. Feng SJ, Chen Q, Gu GH et al. Fringe pattern analysis using deep learning. *Adv Photonics* **1**, 025001 (2019).
18. Yin W, Che YX, Li XS et al. Physics-informed deep learning for fringe pattern analysis. *Opto-Electron Adv* **7**, 230034 (2024).
19. Qian JM, Feng SJ, Li YX et al. Single-shot absolute 3D shape

measurement with deep-learning-based color fringe projection profilometry. *Opt Lett* **45**, 1842–1845 (2020).
20. Qian JM, Feng SJ, Tao TY et al. Deep-learning-enabled geometric constraints and phase unwrapping for single-shot absolute 3D shape measurement. *APL Photonics* **5**, 046105 (2020).
21. Li YX, Qian JM, Feng SJ et al. Deep-learning-enabled dual-frequency composite fringe projection profilometry for single-shot absolute 3D shape measurement. *Opto-Electron Adv* **5**, 210021 (2022).
22. Zuo C, Tao TY, Feng SJ et al. Micro Fourier transform profilometry (*μ*FTP): 3D shape measurement at 10, 000 frames per second. *Opt Lasers Eng* **102**, 70–91 (2018).
23. Heist S, Dietrich P, Landmann M et al. GOBO projection for 3D measurements at highest frame rates: a performance analysis. *Light Sci Appl* **7**, 71 (2018).
24. Baraniuk RG. Compressive sensing [Lecture Notes]. *IEEE Signal Process Mag* **24**, 118–121 (2007).
25. Park J, Gao L. Cascaded compressed-sensing single-pixel camera for high-dimensional optical imaging. *PhotoniX* **5**, 37 (2024).
26. Zhang ZH, Zhang B, Yuan X et al. From compressive sampling to compressive tasking: retrieving semantics in compressed domain with low bandwidth. *PhotoniX* **3**, 19 (2022).
27. Mait JN, Euliss GW, Athale RA. Computational imaging. *Adv Opt Photonics* **10**, 409–483 (2018).
28. Luo Y, Zhao YF, Li JX et al. Computational imaging without a computer: seeing through random diffusers at the speed of light. *eLight* **2**, 4 (2022).
29. Gao L, Liang JY, Li CYet al. Single-shot compressed ultrafast photography at one hundred billion frames per second. *Nature* **516**, 74–77 (2014).
30. Llull P, Liao XJ, Yuan X et al. Coded aperture compressive temporal imaging. *Opt Express* **21**, 10526–10545 (2013).
31. Reddy D, Veeraraghavan A, Chellappa R. P2C2: programmable pixel compressive camera for high speed imaging. In *Proceedings of the CVPR 2011* 329–336 (IEEE, 2011).
32. Yuan X, Brady DJ, Katsaggelos AK. Snapshot compressive imaging: theory, algorithms, and applications. *IEEE Signal Process Mag* **38**, 65–88 (2021).
33. Lin HN, Cheng JX. Computational coherent raman scattering imaging: breaking physical barriers by fusion of advanced instrumentation and data science. *eLight* **3**, 6 (2023).
34. Chen WW, Feng SJ, Yin W et al. Deep-learning-enabled temporally super-resolved multiplexed fringe projection profilometry: high-speed khz 3D imaging with low-speed camera. *PhotoniX* **5**, 25 (2024).
35. Wang BW, Chen WW, Qian JM et al. Single-shot super-resolved fringe projection profilometry (SSSR-FPP): 100, 000 frames-per-second 3D imaging with deep learning. *Light Sci Appl* **14**, 70 (2025).
36. Weise T, Leibe B, Van Gool L. Fast 3D scanning with automatic motion compensation. In *Proceedings of 2007 IEEE Conference on Computer Vision and Pattern Recognition* 1–8 (IEEE, 2007).
37. Tao TY, Chen Q, Da J et al. Real-time 3-D shape measurement with composite phase-shifting fringes and multi-view system. *Opt Express* **24**, 20253–20269 (2016).
38. Bräuer-Burchardt C, Munkelt C, Heinze M et al. Using geometric constraints to solve the point correspondence problem in fringe projection based 3D measuring systems. In *Proceedings of the 16th International Conference on Image Analysis and Processing–ICIAP 2011* 265–274 (Springer, 2011).
39. Li ZW, Zhong K, Li YF et al. Multiview phase shifting: a full-resolution and high-speed 3D measurement framework for arbitrary shape dynamic objects. *Opt Lett* **38**, 1389–1391 (2013).
40. Zuo C, Huang L, Zhang ML et al. Temporal phase unwrapping algorithms for fringe projection profilometry: a comparative review. *Opt Lasers Eng* **85**, 84–103 (2016).
41. Gu JX, Wang ZH, Kuen J et al. Recent advances in convolutional neural networks. *Pattern Recogn* **77**, 354–377 (2018).
42. Feng SJ, Xiao YL, Yin W et al. Fringe-pattern analysis with ensemble deep learning. *Adv Photonics Nexus* **2**, 036010 (2023).
43. Ibtehaz N, Rahman MS. MultiResUNet: rethinking the U-Net architecture for multimodal biomedical image segmentation. *Neural Netw* **121**, 74–87 (2020).
44. Ronneberger O, Fischer P, Brox T. U-Net: convolutional networks for biomedical image segmentation. In *Proceedings of the 18th International Conference on Medical image computing and computer-assisted intervention–MICCAI 2015* 234–241 (Springer, 2015).
45. Kellman MR, Bostan E, Repina NA et al. Physics-based learned design: optimized coded-illumination for quantitative phase imaging. *IEEE Trans Comput Imaging* **5**, 344–353 (2019).
46. Wang F, Bian YM, Wang HC et al. Phase imaging with an untrained neural network. *Light Sci Appl* **9**, 77 (2020).
47. Heist S, Lutzke P, Schmidt I et al. High-speed three-dimensional shape measurement using GOBO projection. *Opt Lasers Eng* **87**, 90–96 (2016).
48. Caspar S, Honegger M, Rinner S et al. High speed fringe projection for fast 3D inspection. *Proc SPIE* **8082**, 80820Y (2011).
49. Lin X, Rivenson Y, Yardimci NT et al. All-optical machine learning using diffractive deep neural networks. *Science* **361**, 1004–1008 (2018).

Acknowledgements

This work was supported by National Key Research and Development Program of China (2022YFB2804603, 2022YFB2804605), National Natural Science Foundation of China (U21B2033), Fundamental Research Funds forthe Central Universities (2023102001, 2024202002), National Key Laboratory of Shock Wave and Detonation Physics (JCKYS2024212111), China Post-doctoral Science Fund (2023T160318), Open Research Fund of JiangsuKey Laboratory of Spectral Imaging & Intelligent Sense (JSGP202105,JSGP202201), and Postgraduate Research & Practice Innovation Program of Jiangsu Province (KYCX25_0695, SJCX25_0188)

Competing interests

The authors declare no competing financial interests.

Supplementary information

Supplementary information and Visualization S1 for this paper is available at https://doi.org/10.29026/oea.2025.250021

Scan for Article PDF